

# Amplified hazard of small-volume monogenetic eruptions due to environmental controls, Orakei Basin, Auckland Volcanic Field, New Zealand

Károly Németh · Shane J. Cronin · Ian E. M. Smith ·  
Javier Agustín Flores

Received: 17 June 2011 / Accepted: 23 August 2012 / Published online: 12 September 2012  
© Springer-Verlag 2012

**Abstract** Orakei maar and tuff ring in the Auckland Volcanic Field is an example of a basaltic volcano in which the style and impacts of the eruption of a small volume of magma were modulated by a fine balance between magma flux and groundwater availability. These conditions were optimised by the pre-85 ka eruption being hosted in a zone of fractured and variably permeable Plio-Pleistocene mudstones and sandstones. Orakei maar represents an end-member in the spectrum of short-lived basaltic volcanoes, where substrate conditions rather than the magmatic volatile content was the dominant factor controlling explosivity and eruption styles. The eruption excavated a crater >80 m deep that was subsequently filled by slumped crater wall material, followed by lacustrine and marine sediments. The explosion crater may have been less than 800 m in diameter, but wall collapse and wave erosion has left a 1,000-m-diameter roughly circular basin. A tuff ring around part of the maar comprises dominantly base surge deposits, along with subordinate fall units. Grain size, texture and shape characteristics indicate a strong influence of magma–water and magma–mud interactions that controlled explosivity throughout the eruption, but also an ongoing secondary role of magmatic gas-driven expansion and fragmentation. The tuff contains >70 % of material recycled from the underlying Plio-Pleistocene sediments, which is strongly predominant in the >2  $\phi$  fraction. The magmatic clasts are evolved alkali basalt, consistent with the eruption of a very small batch of

magma. The environmental impact of this eruption was disproportionately large, when considering the low volume of magma involved ( $DRE < 0.003 \text{ km}^3$ ). Hence, this eruption exemplifies one of the worst-case scenarios for an eruption within the densely populated Auckland City, destroying an area of  $\sim 3 \text{ km}^2$  by crater formation and base surge impact. An equivalent scenario for the same magma conditions without groundwater interaction would yield a scoria/spatter cone with a diameter of 400–550 m, destroying less than a tenth of the area affected by the Orakei event.

**Keywords** Basaltic monogenetic volcanoes · Orakei Basin · Phreatomagmatic eruptions

## Introduction

Monogenetic volcanic systems are expressed at the Earth's surface as fields of individual, short-lived volcanoes, which are commonly but not exclusively small in volume, typically  $< 0.1 \text{ km}^3$  dense rock equivalent (DRE) of erupted deposits (Wood 1980; Valentine and Gregg 2008; Németh 2010). The specific occurrence of eruption types within fields is often related to topography and groundwater conditions, with phreatomagmatic volcanoes common in basin or coastal areas and scoria or spatter cones and lava flows occurring in topographically higher locations (White 1991; Sohn and Park 2005). Other locations for phreatomagmatism include fault zones and other fracture systems that host groundwater, but may not be represented topographically (Lesti et al. 2008).

Despite their small size, basaltic monogenetic volcanoes can be complex, not only in their range of eruption styles, but also geochemically (Houghton et al. 1999; Smith et al. 2008; Brenna et al. 2010). A consequence of their small magma volumes is that the host environment and in particular the hydrogeology of the environment, can exert a strong influence on the style of eruption (Lorenz 2003;

---

Editorial responsibility: J. C. Phillips

K. Németh (✉) · S. J. Cronin · J. Agustín Flores  
Volcanic Risk Solutions, Institute of Natural Resources,  
Massey University,  
Private Bag 11 222,  
Palmerston North, New Zealand  
e-mail: K.Nemeth@massey.ac.nz

I. E. M. Smith  
School of Environment, The University of Auckland,  
Auckland, New Zealand

Ross et al. 2011). In addition, the availability of surface water, in part a function of climate, plays an important role in determining eruption mechanisms and resulting volcanic landforms (e.g. Carn 2000). Under optimum magma–water interaction conditions, explosive phreatomagmatic eruptions produce wide, low-profile cones with deep craters, surrounded by tuff rings formed from stacked deposits of pyroclastic density currents and tephra falls (Dellino et al. 1990; White and Ross 2011). The shape of the landform is strongly dependent on the nature of the pre-eruptive surface, the lithology and mechanical properties of the country rock vent geometry, and the availability of external water (Lorenz 2003). Soft substrates (generally young muds, sands and poorly consolidated, fine-grained sedimentary rocks) engender magma–mud interactions and phreatomagmatic activity is primarily controlled by the availability of pore water (Lorenz 2003; Sohn and Park 2005; Auer et al. 2007). In the case of hard rock substrates (e.g. lava fields, indurated clastic sediment, limestone and plutonic rocks) water is stored in macro-scale fractures and cavities that can quickly recharge, causing phreatomagmatic eruptions to carve out steep-sided, deep maars, underlain by deep-seated diatremes.

At the smallest scale of volcanic systems, and under the lowest magma flux rates, near-surface environments have the greatest potential to influence eruption processes. In long and large-volume eruptions of the Auckland Volcanic Field (AVF), an evolution often occurs from initial phreatomagmatic eruptive phases, followed by Strombolian or Hawaiian eruptions, fire-fountains and in some cases lava flows (Allen and Smith 1994). This reflects a declining influence of magma–groundwater interaction with time. More-rapid and reversible changes in eruption style may also occur, due either to changes in magma flux (e.g. Sohn et al. 2012), or to external influences. These conditions may be indicated by scoria fall deposits that are interbedded within phreatomagmatic tuff ring successions, reflecting periods when water availability was suppressed (Houghton et al. 1999). Simultaneous magmatic and phreatomagmatic explosions may also occur from adjacent vents, as evidenced from deposits in the Eifel Volcanic Field (Houghton and Schmincke 1986) or Crater Hill (AVF, NZ) (Houghton et al. 1999).

In this paper, we report a study of the volcanic facies architecture of Orakei volcano, Auckland Volcanic Field, New Zealand which was undertaken to examine the conditions and hazard potential of the smallest possible magma volume eruptions in the field. In this case, the erupted magma volume was estimated to be less than  $0.01 \text{ km}^3$  DRE (Allen and Smith 1994) and thus it might be expected to have formed one of the smallest volcanic structures of the field. Instead, it created an almost 1-km-diameter basin, with an inset maar, surrounded by a broad tuff ring and widespread pyroclastic deposits. Future eruptions of this type are

one of the most hazardous scenarios expected for the >1.4 million inhabitants of Auckland City. Here, we examine the hypothesis that the explosivity and impacts of this eruption were so great because of favourable host conditions such as optimal groundwater availability and recharge rate and country rock properties. Under optimum conditions, as represented by the Orakei eruption, magma–water interaction is extremely explosive and dominates eruption properties.

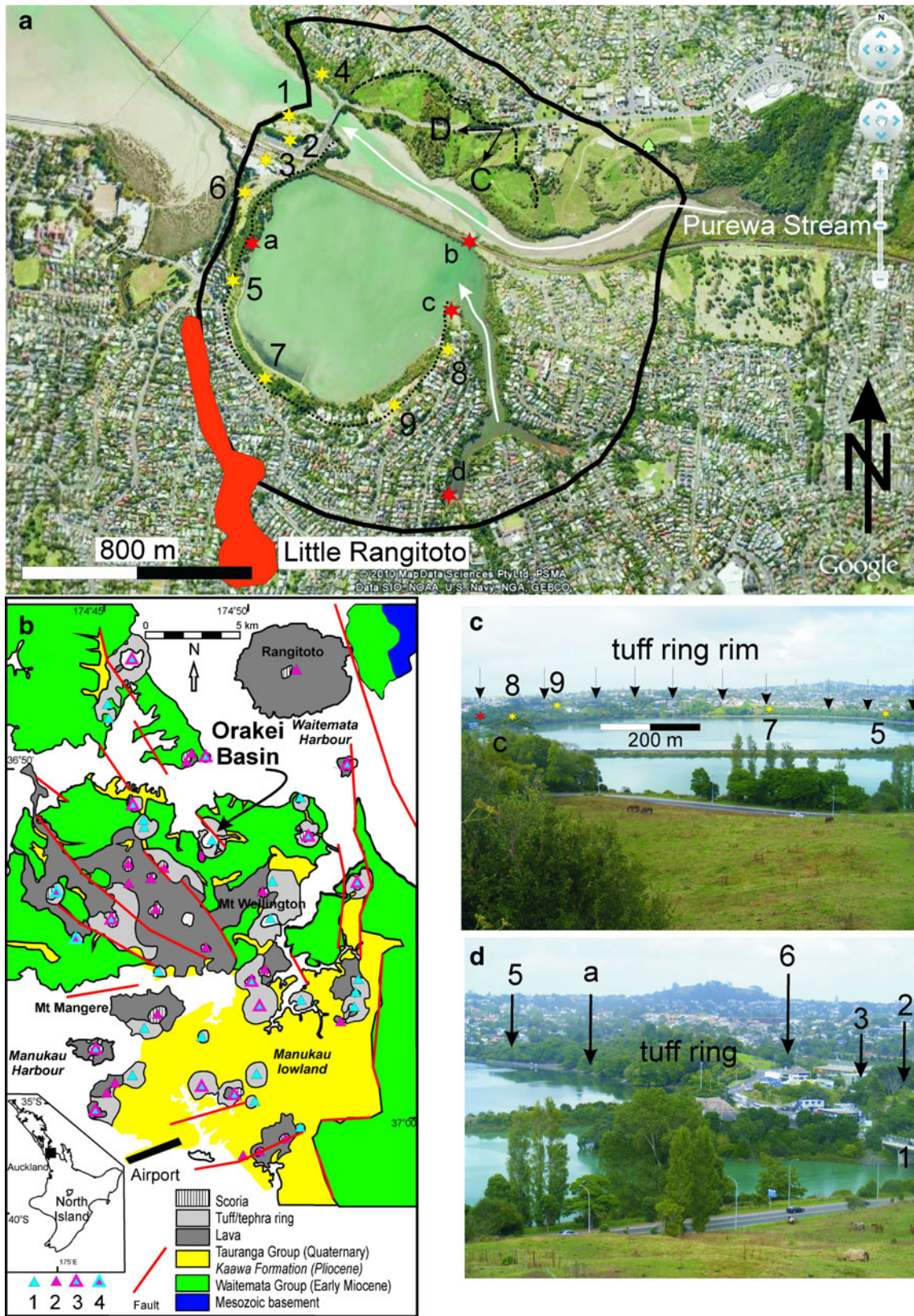
### Orakei, Auckland volcanic field

The Orakei volcano (Fig. 1a) is one of the older eruptive centres in the Auckland Volcanic Field (Fig. 1b) (Allen et al. 1996; Bebbington and Cronin 2011). A core recovered from the upper 80 m of the sedimentary infill of the basin showed a near-continuous sequence of estuarine and paleo-lake deposits with a minimum age of 85,000 years estimated from tephrochronology and extrapolated sediment deposition rates (Molloy et al. 2009). Geophysical study suggests there is no lava infill in this crater (Cassidy et al. 2007), hence essentially all of the magma was erupted as juvenile pyroclasts within the tuff ring (Fig. 1c). The edges of the crater expose the substrate Waitemata Formation (weakly lithified Miocene siliclastic sandstone/mudstones; Edbrooke et al. 2003), at ~6 m above sea level inside the western edge of the crater (Fig. 1d). Inward collapse of the tuff ring partly filled the basin and extended the basin rim to its present-day c. 1,000 m diameter (Fig. 1a). Rapid modification of the tuff ring morphology after its formation is expected through gully formation and wave cut erosion as has been documented at other young coastal maars including of Ambrym AD 1913 eruption in Vanuatu (Németh and Cronin 2007). However, the timing of post-eruptive crater enlargement over long time-scales (thousands of years) is poorly

**Fig. 1** **a** Orakei maar on a Google Earth satellite image. *Thick black line* marks the lateral extent of pyroclastic deposits of the maar. *Red field* shows the Little Rangitoto scoria cone and associated lava flow in the SW of the Orakei maar. *White arrows* show the flow direction of small streams entering to the maar basin. *Thin dashed black line* in the northern edge represents a region of landslides. *Thin black arrows* with capital letters of *C* and *D* show the views that were taken on **c** and **d**. *Numbers with yellow stars* represent locations of type sections shown on Fig. 2. *Thin black dotted line* is the location of the present-day escarpment of the maar inner crater wall. *Letter a with red star* marks the location of benches about 6 m above the present-day sea level. The locations marked with *b* and *c* are the places where unconformity surfaces have been identified. Location *d* marks a place where a narrow stream breached the outer crater rim of the maar. **b** Location of the Auckland Volcanic Field and Orakei Basin. Volcano types 1 dominant major phreatomagmatic volcano, 2 dominant major magmatic volcano, 3 major phreatomagmatic volcano with various magmatic infill, 4 dominantly magmatic volcano with phreatomagmatic influence in some stage of its eruption. **c** Panoramic view of the Orakei Basin from the north. *Arrows* point to the tuff ring crest. *Numbers* refer to sample and/or log locations (see text). **d** View over the outflow of the breached maar from its NE edge. *Numbers and letter* refer to the locations shown on **a**

constrained; it could have been continuous due to lake level fluctuation, diatreme settling, diagenetic processes and

anthropogenic modifications (e.g. Suhr et al. 2006). The Orakei maar was formed in a valley and was subsequently



eroded by the Purewa Stream (Fig. 1a). Pyroclastic deposits to the north were emplaced on a steep paleovalley flank and subsequent slumping and soil creep has destroyed the tuff ring geomorphology of this portion (Fig. 1a). The most intact and distinctive remnants of the 10–40-m-high tuff ring are preserved around the SW–SE–E sectors of Orakei maar (Fig. 1a, c & d).

The exposed pyroclastic deposits of the Orakei tuff ring represent the outer depositional flanks of the volcanic structure (Fig. 1c) and dip radially outward from the basin centre at 5–10°. The only exception is at the NW crater rim, where beds dip toward the crater centre, indicating the original position of part of the inner crater wall. More subtle variations in dip direction and angle were influenced by the NW–SE trending paleovalley of the Purewa Stream, marked by elevated ridges of sedimentary rocks (Fig. 1a).

### Characteristics of the pyroclastic succession

There are few outcrops exposing >4 m of the succession, but lateral correlation of individual units is possible by matching distinctive pyroclastic packages (Fig. 2). The deposits, especially the finest ash-dominated beds, are typically indurated. The thickest successions occur on the eastern side of the maar and include unconformities indicating where strata

have collapsed inward. Ten locations around the tuff ring are described (Fig. 2), with their elevation above sea level corresponding roughly to stratigraphic position. The basal units consist dominantly of pyroclastic breccias and lapilli tuff beds. These are overlain by a uniform lapilli tuff and tuff succession that grades upward into thinner, well-defined beds. In the uppermost section, coarser lapilli tuffs occur that are strongly weathered and friable.

### Basal deposits

The lowermost pyroclastic sequences (at sea level in places), consist of coarse, flat-lying and massive tuff breccia beds up to 50 cm thick and interbedded with thin (1–3 cm) pale brownish grey fine tuffs. These are restricted to the north-western side of the basin, where the tuff ring remnant forms a small peninsula (Fig. 1a). In radially oriented sections, the tuff breccia units total ~3 m in thickness (Fig. 3a). These pass upward into a sequence of 10-cm scale, coarse lapilli tuff beds, interbedded with fine tuff, grading further upward into a regularly bedded rhythmic succession of fine tuff and lapilli tuff with occasional dense lava blocks. The fine brownish grey/grey tuff units are similar in all parts of this sequence.

The tuff breccias contain up to 20 % by volume (visual estimates from outcrop and hand specimens) sedimentary

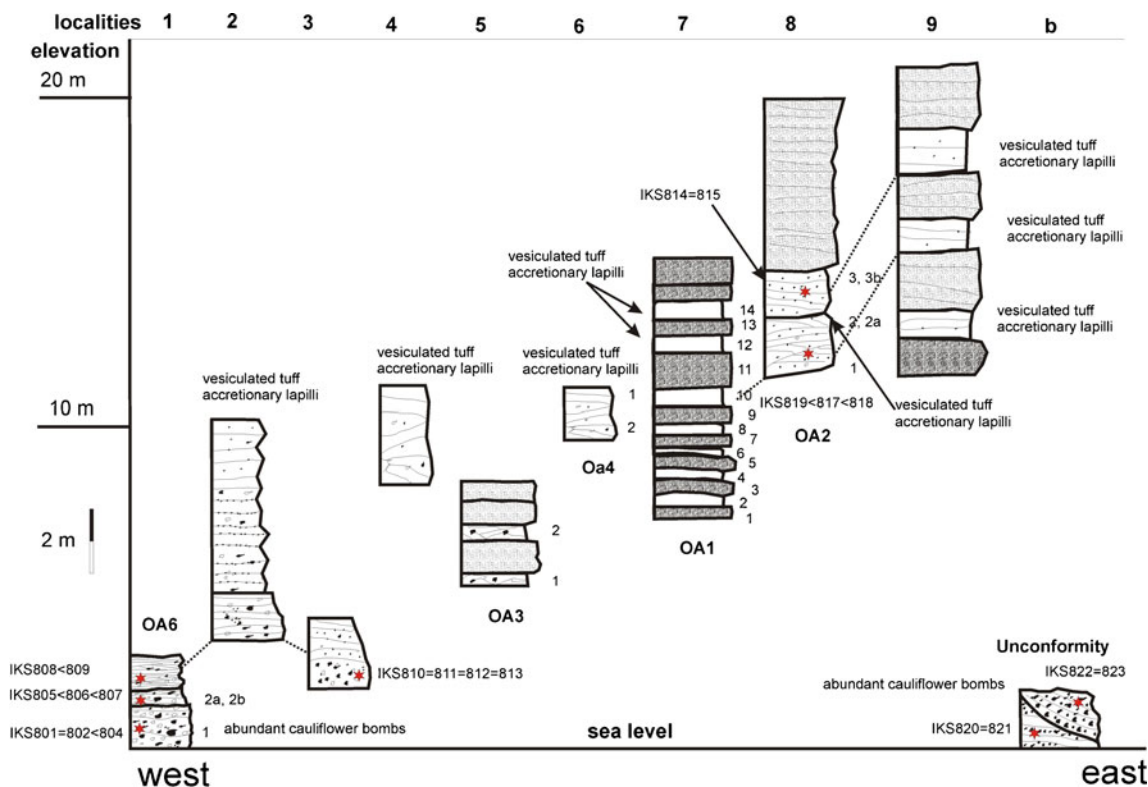


**Fig. 2** Stratigraphy logs across the Orakei maar. *Numbers* refer to the locations marked on Fig. 1a. *Stars* refer to the samples from where juvenile lapilli have been collected for whole-rock chemical analysis (field names of samples listed next to logs)

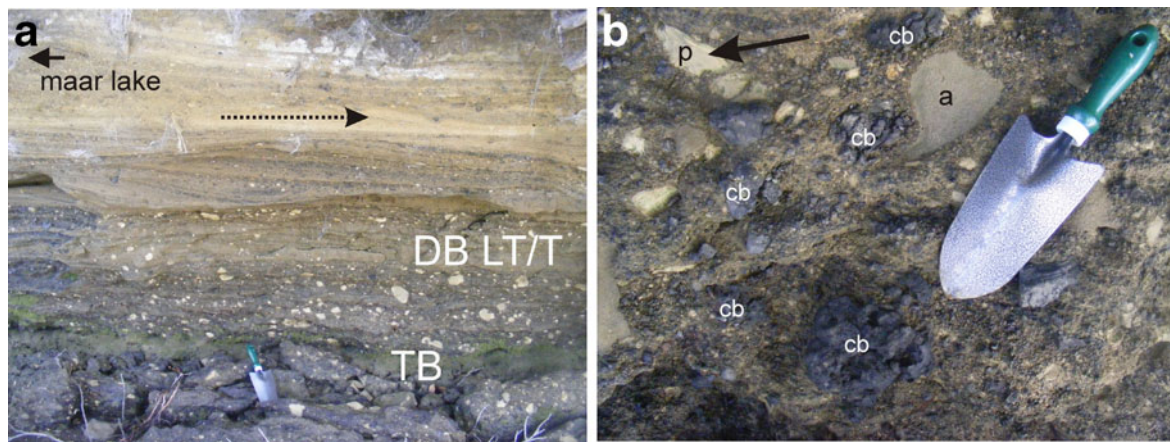


**Fig. 3** **a** The basal pyroclastic rock units (photograph was taken about 300 m from the maar crater rim) are rich in accidental lithic fragments derived from the immediately underlying siliciclastic rock units. The base of the sequence is a tuff breccia (*TB*) that is interbedded with dune-bedded lapilli tuff and tuff successions rich in fine-grained

accidental lithic fragments. *Dashed arrow* shows the inferred transportation direction of the base surge that deposited these units. **b** Close up of the basal tuff breccias that are rich in cauliflower bombs (*cb*), accidental lithic fragments (*a*), and plastically deformed mud (*an arrow points to a clast marked with p*)

clasts, including blocks up to 50 cm in diameter (Fig. 3a). Many of these clasts preserve original sedimentary textures and show fractures or fracture-bounded margins. The sedimentary clasts are not thermally altered, but some are mechanically milled and deformed (Fig. 3b).

Juvenile magmatic fragments are commonly ribbon-like, dense to poorly vesicular basalt, which universally contains common mud inclusions of 0.5–2 cm in diameter that are homogenised and moderately thermally altered. The matrix of the tuff breccia contains >70 vol.% sedimentary grains (visual estimates on hand specimens and thin sections), with the remainder being angular, poorly vesicular basaltic glassy fragments (Fig. 3a).

The basal tuff breccia exhibits textural features that are characteristic of pyroclastic deposits formed during the vent-opening stages of a phreatomagmatic eruption (c.f. White and Ross 2011). Its crudely stratified nature indicates transportation by high-particle concentration pyroclastic density currents (proximal base surges) and/or transformed debris flows, along with debris jets in which large clasts were blasted toward their depositional sites (e.g. Ross and White 2006). Some juvenile and non-volcanic particles were also transported as ballistics, causing impact sags in the freshly deposited beds that must have been soft and wet. The lack of alteration or baking of the large non-volcanic clasts indicates that overall temperatures reached during fragmentation were low, or that magma–host contact was brief. Low emplacement temperatures are also shown by sedimentary features resulting from condensed water in the base surges (accretionary lapilli, vesicular internal textures and soft-sediment deformation features).

The ubiquitous and common presence of sediment (mud) blebs peppered throughout juvenile lapilli and bombs provides evidence for intimate mingling of magma with

unconsolidated country “rock” during the early phases of this eruption. Large juvenile particles are dominantly cauliflower-shaped bombs that were not deformed on impact. Other large bombs are dense and glassy with angular shapes commonly exhibiting jig-saw cooling fractures. While the lowest beds record a rapid vent-clearing/excavation phase (with abundant blocks and impact sags), these pass rapidly to well-defined alternating lapilli and ash tuff beds, indicating stable vent/conduit conditions with regular rhythmic explosive eruptions driven by magma–water or magma–mud interaction. These bedding characteristics, including dune forms with cross-bedding on a length scale of 1.5–2 m, imply base surge deposition.

#### Medial to upper pyroclastic succession

The medial sections of the north-western rim show a sequence of low-angle, almost flat-lying, alternating coarse to fine-lapilli tuff and fine tuff beds (Fig. 4a). These are cross-bedded in some cases, planar bedded in others and dominated by accidental fragments from the sedimentary host rocks. Juvenile fragments are dominantly angular, glassy and poorly vesicular, but include rare, frothy, highly vesicular coarse ash and lapilli (Fig. 4a). Juvenile lapilli are commonly coated by millimeter-thick films of mud. The 2–10-cm-thick fine tuff beds are commonly vesicular and rich in rim-type accretionary lapilli (with a distinct core and well-distinguished concentric external layers, e.g. Brown et al. 2010), along with irregularly shaped mud aggregates, containing as little as 25 % by volume juvenile fragments (estimated from thin sections). The fine tuff beds intercalate with decimeter-scale packages of wavy and dune-bedded lapilli tuff that may contain up to 75 % vesicular juvenile lapilli. The fine-grained tuff packages become dominant up-

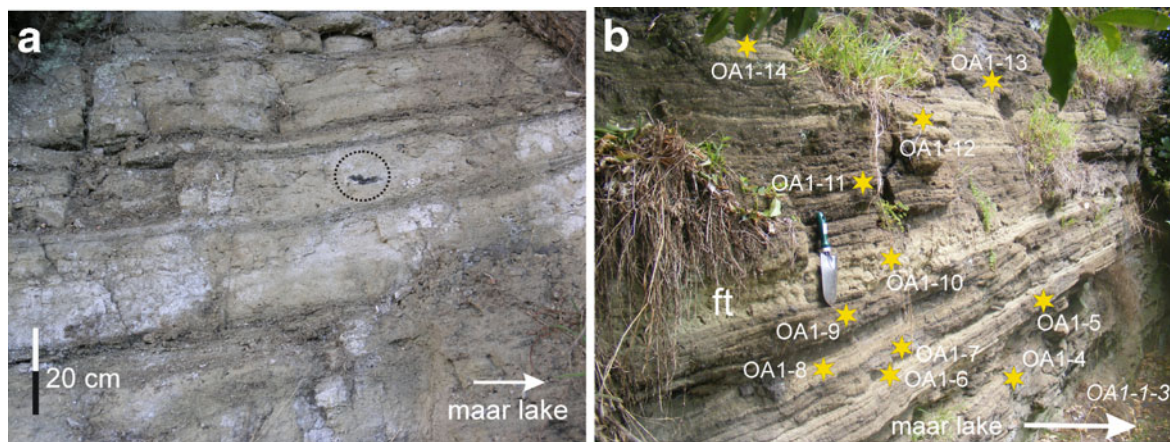


**Fig. 4** **a** Section across the medial (in sense of stratigraphic position) pyroclastic succession of the Orakei maar about 100 m from the maar crater rim. It consists of a fine-grained, accidental lithic-rich tuff (*light colour*) interbedded with thin juvenile pyroclast rich beds (*dark layer*). The fine-grained tuff occasionally contains very frothy juvenile lapilli with rugged shapes (*dashed circle*). **b** Upper section of the Orakei maar

with fine tuff layers (*ft*) rich in fine silt and mud from the present-day crater wall escarpment. Such fine-grained tuff is commonly vesicular and contains rim-type accretionary lapilli. Stars are the locations from where samples were collected for grain size and juvenile pyroclast shape analysis. *Sample names* are listed next to the stars

section, with occasional coarse lapilli, bombs and blocks forming impact sags (Fig. 4b).

This sequence reflects continuation of a regular pulsating explosive phreatomagmatic eruption with a stable vent zone. The common mud coatings indicate that much of the fuel–coolant interaction was a mud–magma interaction, similar to eruptions described by Kienle et al. (1980) and Ort et al. (2000). Pulsating explosive eruptions produced base surges and fine-ash falls. No major disturbances caused by crater collapse/choking or vent migration are indicated (e.g. by ballistic bomb/block horizons and breccias). Beds rich in vesicular juvenile lapilli indicate periods when magma–water interaction was weak and magmatic gas-driven expansion and fragmentation dominated. This may reflect a peak in the magma flux. The upward increase in abundance of very fine-grained, juvenile-poor, dune-bedded vesicular and accretionary lapilli-bearing tuffs represents a return to highly energetic phreatomagmatic eruptions (e.g. close to an optimal magma–coolant interaction ratio), displacing mud from the vent zone.

#### Capping pyroclastic successions

The uppermost deposits are strongly weathered (Fig. 4b) and grade upward from coarse ash tuffs to decimeter-scale fine-lapilli tuff beds. These units contain the highest content of vesicular juvenile lapilli of the entire sequence (~75 vol%; estimated from outcrop and hand specimens). The lapilli have higher vesicularity than those down-section, indicating greater magmatic gas expansion before fragmentation. No complete drying of the eruption is evidenced, as has occurred at many other Auckland volcanoes (e.g. Allen et al. 1996).

#### Unconformity surfaces

In basal exposures inside the eastern side of the tuff ring, an irregular angular unconformity, dipping inward, separates two packages of lapilli tuffs composed dominantly of base surge deposits (Fig. 5a). The lower package dips gently outward from the crater and shows syn-depositional faulting, while the upper, texturally similar unit has a higher juvenile content and is flat-lying. A similar unconformity at the same stratigraphic level occurs 300 m to the north (Fig. 5b), where faulted lapilli tuff successions dip outward and pass up through an irregular contact to fine-grained tuff with subhorizontal bedding.

These unconformity surfaces possibly indicate either a shift of the erupting vent by a few tens of metres during the eruption, or vent widening. Vent shifting and widening is common to basaltic phreatomagmatic volcanoes (Sohn and Park 2005) and may relate to changes in the magma supply (Sohn et al. 2012). A magmatic change or a vent-pathway change may alter eruption/fragmentation dynamics and resultant deposits (Brand and Clarke 2009).

#### Pyroclastic textures and particles

Bulk tephra samples were collected at five locations (Figs 1, 2), disaggregated in weak acid (HCl 10 mol. %) and dried. They were dry sieved in half  $\phi$  classes between  $-5.5$  and  $5$   $\phi$ . The  $>5$   $\phi$  class is large for fine tuff samples. For each grain-size class, the juvenile particle content was counted (at least 200 individual particles) under a reflected-light microscope.

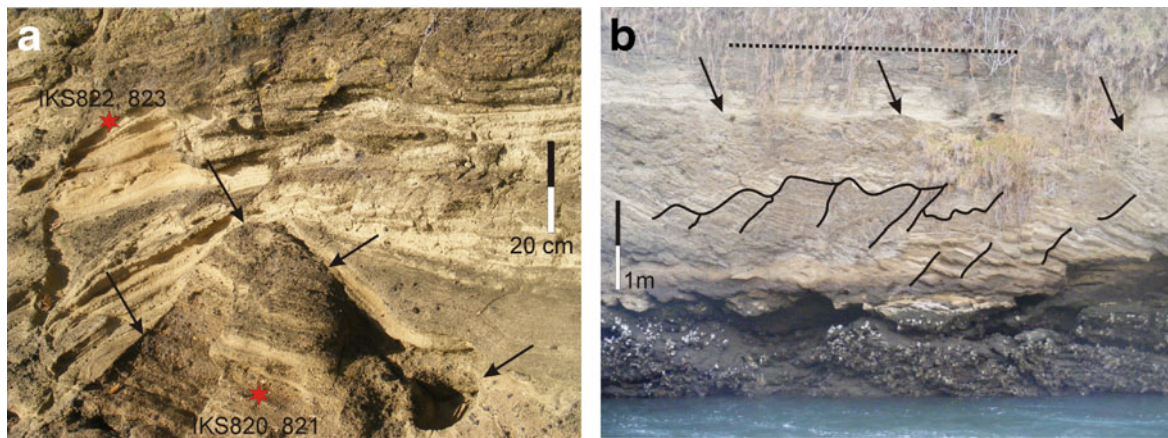


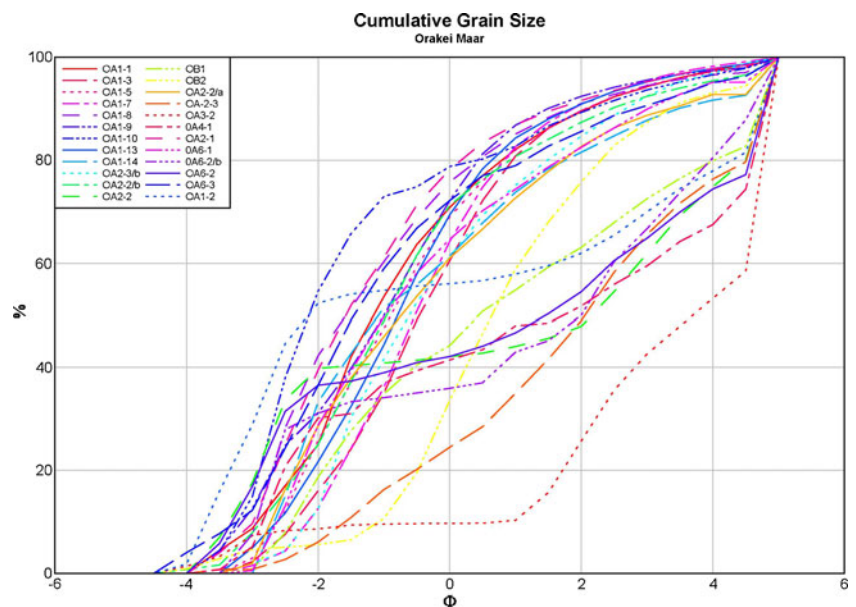
**Fig. 5** **a** An unconformity surface (*arrows*) in the location marked with *c* on Fig. 1a. *Numbers* refer to samples collected for chemical analysis. **b** Major unconformity surface (*arrows*) in the northern side of the maar, near the maar lake level, about 300 m north from the previous

location shown on **a**. *Black outlines* represent faulted blocks in the lower unit, while the *dashed line* shows the subhorizontal bedding above the unconformity surface

The basal tuff breccias at all locations have a unimodal grain-size distribution, strongly coarse-skewed. The overlying pyroclastic beds show two types (Fig. 6): (1) mantle-bedded units with unimodal grain-size distributions, which are likely to be fall deposits or basal traction carpets deposited from density-stratified base surges (e.g. Dellino et al. 2004a, b; Valentine 1987), and (2) pinching and swelling, dune-bedded poorly sorted beds with grain-size distributions skewed toward the finer classes, most likely deposited by base surges.

The basal tuff breccias have a high non-volcanic content. All other beds of the middle to upper sequence contain >90 vol% juvenile pyroclasts in coarse fractions (<2  $\phi$ ), but no more than 10 % in fine (>2  $\phi$ ) fractions (Fig. 6). The fine-ash non-volcanic particles include mudstone-derived quartz and clay-minerals, pyroxene, feldspar and muscovite.

**Fig. 6** Cumulative grain-size distribution diagram on sieved samples from the pyroclastic succession of Orakei maar. OA1-1,3,5,7,9, and 13 are beds that are well-sorted and deposited by fall-dominated processes or traction carpet deposition from a density-stratified base surge, while the rest of the samples represent beds that are clearly originate from base surge originated



Pyroclast morphology

Sieved particles were cleaned in water in an ultrasonic bath before scanning electron microscopy (SEM) at the Manawatu Microscopy Centre at Massey University on an FEI Quanta 200 SEM operated under 20 kV acceleration. Juvenile pyroclasts commonly show cracked surfaces and coatings of non-volcanic dust/mud (Fig. 7). They often have extensive palagonitisation, shown by alteration of glass to a pale brown opaque state. Palagonitisation is more advanced in the coarser grained juvenile particles, which are altered at their rims and along fractures through the glassy lapilli and coarse ash (Fig. 7c & d). The coarser than 2  $\phi$  juvenile pyroclasts are commonly microvesicular (Fig. 7f) with irregularly shaped vesicles, showing thick walls, with smooth (Fig. 7f) surfaces, often forming a peel-like texture (Fig. 7e). Non-altered

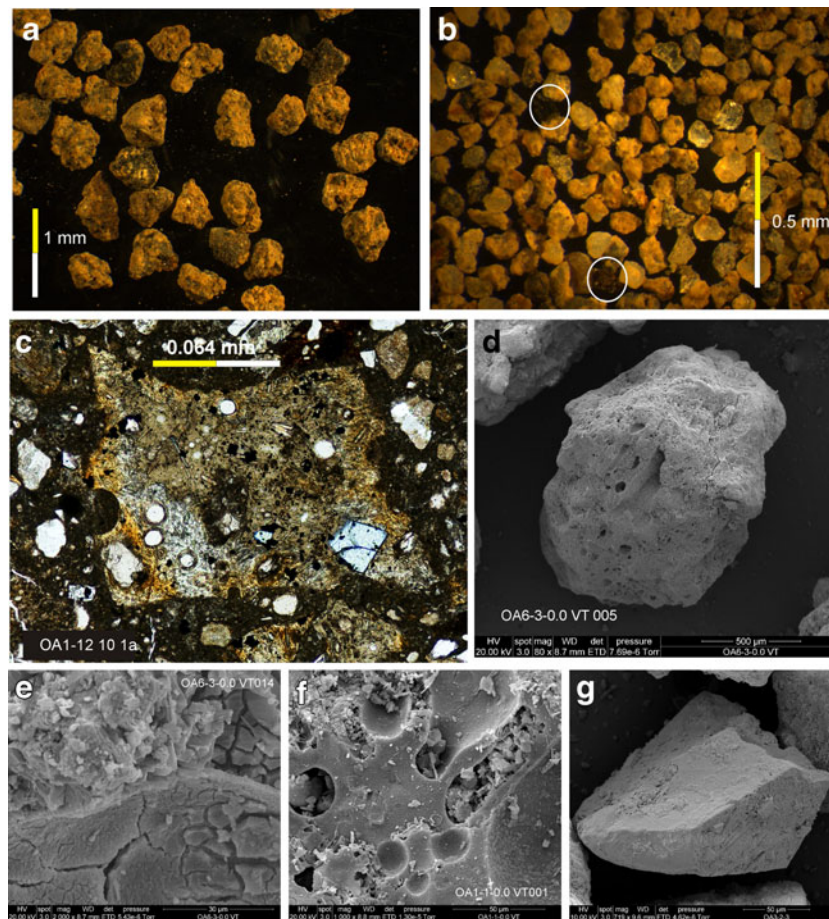


**Fig. 7** Microtextures of juvenile pyroclasts from the pyroclastic succession of the Orakei maar: **a** light microscopy image of coarse ash fraction of a sample from the medial section of the Orakei maar sequence dominated by moderately vesicular glassy pyroclast commonly covered by thin ash rim. **b** The fine fraction of the majority of the pyroclastic deposits of Orakei maar is dominated by non-volcanic lithic fragments of sand and silt. Juvenile ash is rare (*white circle*). **c** Thin section image (*plane parallel light*) of typical blocky glassy

pyroclasts from the upper section of the pyroclastic rock units of Orakei maar. Glassy pyroclasts are moderately to non-vesicular but commonly rich in microlites that provide trachytic texture to the glass shards. **d** Scanning electron microscope image of a moderately vesicular coarse ash particle. **e** SEM image showing thin cracks on the outer surface of glass shards. **f** SEM image of a typical glass shard showing low vesicularity, and smooth inner surfaces of thick bubble walls. **g** SEM image of a blocky shaped glassy fine-ash particle

juvenile fine-ash particles are typically glassy and angular with sharp edges (Fig. 7g).

Basic morphological parameters of juvenile pyroclasts were determined from binarised 2D optical and SEM photomicrographs using ImageJ software (<http://rsbweb.nih.gov/ij/>). To determine particle shape parameters the same methodology was used as in previous studies of glassy pyroclasts (Dellino and La Volpe 1996). Advanced palagonitisation and particle aggregation precluded analysis from two of the five locations. Measurement of fractal dimensions was used to classify the outline shapes of fresh glassy pyroclasts (following Carey et al. 2000; Dellino and Liotino 2002). Fractal properties in this case measure the extent to which an object's morphological structure is the same, regardless of the scale at which it is viewed. Therefore, it can be used as a quantitative expression

of the complexity of a particle boundary. The “calliper or ruler dimension method” (e.g. Mandelbrot 1967) applies a series of linear step lengths to approximate the total particle perimeter ( $P$ ). As the step length ( $L$ ) reduces, the shape of an irregular boundary is more accurately reproduced. On a plot of  $\log L$  vs.  $\log P$ , (Mandelbrot–Richardson plot; Mandelbrot 1967), a straight line indicates a particle with a self-similar or true fractal shape. The fractal dimension ( $D$ ), is related to the slope,  $S$  of the  $\log L$  versus  $\log P$  plot by:

$$D = 1 - S \quad (1)$$

Values of  $D$  range from 1.0 to 2.0, with higher values corresponding to a more irregular boundary. Here we calculated the longest step length ( $L$ ) and took 40, 50 and 70 % of this, with the minimum defined as 20 pixels for each image



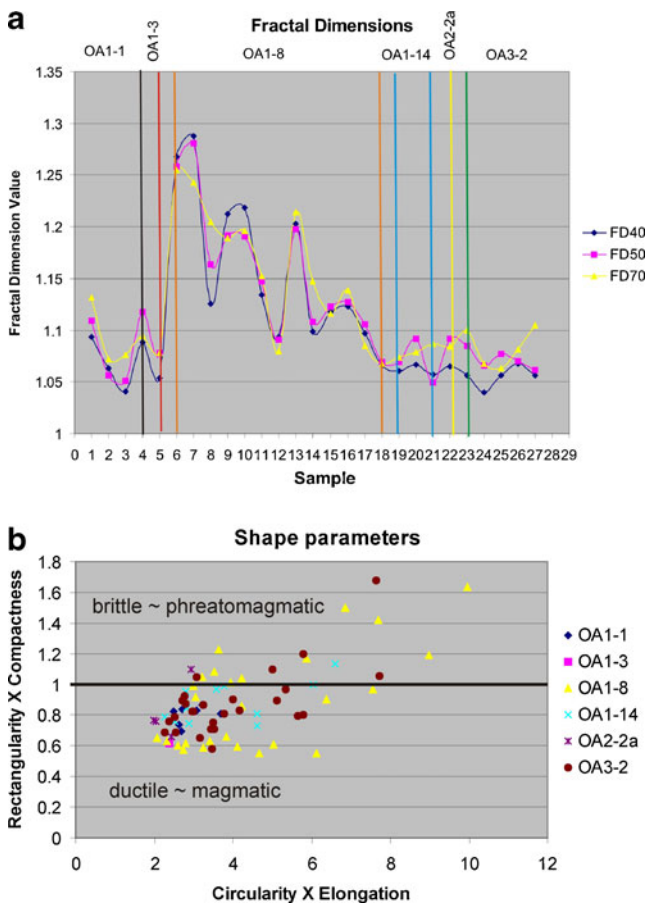


**Fig. 8** **a** Fractal dimensions of measured juvenile glassy pyroclasts from various samples (sample names listed in the upper edge of the diagram). FD40, 50 and 70 refer to the maximum step length used for the fractal dimension calculation as 40, 50 and 70 % of the long axis of the particle. **b** Shape parameter discrimination diagram on the measured juvenile pyroclasts. Note that the majority of the pyroclasts plot near the *rectangularity times compactness* discrimination value of 1, defined by Büttner et al (2002), to separate clast shapes formed by brittle versus ductile deformation

(Fig. 8a). Particles' fractal dimensions were measured using Benoit software ([www.benoit.com](http://www.benoit.com)), which is a user-friendly package to measure quickly various types of fractal dimensions on binary images.

Other particle shape parameters include compactness ( $Q$ ) (the ratio of the particle area and breadth multiplied by width), elongation ( $E$ ) (the ratio of the Feret-diameter—the long axis of an object—and the mean width in a plane perpendicular to the Feret-diameter), circularity ( $C$ ) (the ratio of the particle perimeter and the perimeter of a circle of the same area), and rectangularity ( $R$ ) (the ratio of the particle diameter and twice the sum of the particle breadth and width) following Büttner et al. (2002). On a plot of  $C \times E$  vs.  $R \times Q$  (Fig. 8b) an  $R \times Q$  value of 1 marks a boundary between particles inferred to be shaped by ductile ( $<1$ ) versus brittle ( $>1$ ) fragmentation (Fig. 8b).

Orakei basin glassy juvenile pyroclasts in each grain-size fraction are equant with cracked surfaces. The particles have a wide range in fractal dimensionality ( $D=1.05–1.3$ ), with the most complex shapes resembling the fractal dimensions of a snow-flake ( $D=1.262$ ) (Fig. 8a). Coarse ash particles from throughout the sequence plot uniformly in the ductile field of the Büttner et al. (2002) plot (Fig. 8b), while the fine-ash particles plot in the brittle field. This implies that fine-ash particles were fractured directly by an explosive magma/water interaction, while coarse ash grains were more strongly fragmented by magmatic gas expansion (c.f. Dellino and Liotino 2002). The co-existence of both particle types in the same bed reflects the fine balance between magma flux, expansion and magma–water interaction during the Orakei eruption. Fine-lapilli tuff samples from basal pyroclastic successions show this same pattern (Fig. 8b), implying that both types of fragmentation occurred from the earliest stages of the eruption.

### Pyroclast geochemistry

To assess the behaviour of the magma throughout the Orakei Basin eruption, basaltic bombs and coarse lapilli were collected throughout the sequence (Fig. 2). Basaltic clasts contain subhedral and skeletal olivine and subordinate clinopyroxene microphenocrysts in a groundmass of clinopyroxene and iron-titanium oxide, with or without plagioclase, in vesicular tachylite to sideromelane glass. Clinopyroxene microphenocrysts sometimes occur as radiating or simple glomerocrysts and individual crystals may show sector zoning. Glass and phenocrysts are generally unaltered. Juvenile clasts are increasingly finer-grained and altered up-section, hence the number of bombs suitable for analysis decreased. Bombs sampled had cauliflower shapes, with homogeneous black glassy interiors reflecting sudden cooling. All contained common blebs and enclaves of baked mud, and purely magmatic samples were carefully hand-picked from rock-chips during crushing and before milling. Glass shards were separated from fine tuff beds about 10 m above the present-day water level at localities #7 and #8 (Fig. 1).

The chemical data set comprises major element analyses of glass shards in ash, interstitial glass in basaltic clasts and major and trace element analyses of bulk samples. Glass compositions (Table 1) were measured using the Jeol JXA-840A electron microprobe (EMP) at the University of Auckland.

Analytical data were gathered using a Princeton Gamma Tech Prism 2000 Si (Li) EDS X-ray detector with an electron beam defocused to 5 to 25  $\mu\text{m}$ , under an accelerating voltage of 15 kV, a beam current of 800 pA and 100 s live count time. The ZAF correction method was used to recalculate oxide values. The totals of each measurement were

**Table 1** Spot measurements of volcanic glass compositions measured by using the Jeol JXA-840A electron microprobe (EMP) at the University of Auckland

		10-OA2-1										7-OA1-8																				
		Glass1	Glass1 (unifocus)	Glass2	Glass3	Glass4	Glass5	Glass6	Glass7	Glass8	Glass9	Glass1	Glass2	Glass3	Glass4	Glass5	Glass6	Glass7	Glass8	Glass9	Glass10	Glass1	Glass2	Glass3	Glass4	Glass5	Glass6	Glass7	Glass8	Glass9	Glass10	
1	SiO <sub>2</sub>	41.42	42.04	41.41	41.54	41.74	41.19	42.61	41.21	42.16	40.23	42.38	41.33	3.19	3.23	41.95	43.54	42.39	41.75	42.55	44.98	42.38	41.33	3.19	3.23	41.95	43.54	42.39	41.75	42.55	44.98	
	TiO <sub>2</sub>	3.17	3.18	3.4	3.1	3.33	3.46	3.3	3.22	3.39	4.36	3.02	3.19	3.23	3.2	2.45	3.12	3.43	3.43	3.5	2.21	3.02	3.19	3.23	3.2	2.45	3.12	3.43	3.5	2.21		
	Al <sub>2</sub> O <sub>3</sub>	13.76	14.3	14.27	14.41	14.5	13.7	14.66	14.31	14.3	13.37	14.92	14.1	14.17	14.43	15.74	14.49	14.49	14.15	11.76	15.54	14.92	14.1	14.17	14.43	15.74	14.49	14.15	11.76	15.54		
	FeO	11.27	11.07	12	11.91	12.21	11.12	11.98	11.83	12.22	14.32	12.28	10.5	11.49	11.96	12.31	11.34	12.18	12.18	10.72	10.79	12.28	10.5	11.49	11.96	12.31	11.34	12.18	12.18	10.72	10.79	
	MnO	0.07	0.2	0.1	0.29	0.17	0.13	0.2	0.12	0.21	0.07	0.29	0.2	0.24	0.17	0.33	0.22	0.22	0.22	0.13	0.19	0.29	0.2	0.24	0.17	0.33	0.22	0.22	0.13	0.19		
	MgO	5.04	4.27	4.12	3.94	4.15	4.63	3.96	4.2	4.24	5.2	3.82	4.22	4.47	4.11	3.17	4.24	4.13	4.13	6.5	3.6	3.82	4.22	4.47	4.11	3.17	4.24	4.13	6.5	3.6		
	CaO	13.48	11.75	11.29	10.64	11.06	12.28	11.25	11.07	11.83	12.67	10.62	13.66	11.98	11.26	8.95	11.32	11.32	11.24	15.13	9.94	10.62	13.66	11.98	11.26	8.95	11.32	11.24	15.13	9.94		
	Na <sub>2</sub> O	3.95	4.7	5.28	5.34	5.04	4.44	5.21	4.87	4.82	4.23	6	4.79	4.41	5.38	6.49	5.85	6.18	4.19	5.12	6	6	4.79	4.41	5.38	6.49	5.85	6.18	4.19	5.12		
	K <sub>2</sub> O	1.9	2.38	2.39	2.52	2.54	2.2	2.57	2.42	2.52	2.03	2.86	2.44	2.39	2.62	3.17	2.71	2.39	1.69	1.69	2.86	2.86	2.44	2.39	2.62	3.17	2.71	2.39	1.69	1.69		
	P <sub>2</sub> O <sub>5</sub>	1.92	1.85	1.87	1.72	1.65	1.79	2.07	1.92	1.85	1.32	2.21	1.96	1.98	2.26	2.1	1.96	1.93	1.06	1.45	2.21	2.21	1.98	1.98	2.26	2.1	1.96	1.93	1.06	1.45		
	SO <sub>3</sub>	0.26	0.32	0.18	0.34	0.29	0.09	0.44	0.32	0.5	0.26	0.51	0.35	0.53	0.33	0.35	0.36	0.44	0.17	0.27	0.51	0.51	0.35	0.53	0.33	0.35	0.36	0.44	0.17	0.27		
	Cl	0.12	0.14	0.14	0.16	0.12	0.1	0.12	0.12	0.1	0.09	0.14	0.14	0.14	0.15	0.13	0.13	0.05	0.09	0.1	0.14	0.14	0.14	0.14	0.15	0.13	0.13	0.05	0.09	0.1		
	Cr <sub>2</sub> O <sub>3</sub>	0.12	-0.01	0.15	0.13	0.08	0.06	0.04	0.04	0.1	0.17	0.12	0.12	0.12	0.12	0.12	0.12	0.12	0.12	0.09	0.1	-0.03	0.14	0.16	0.16	0.12	0.12	0.12	0.12	0.12	0.1	
	NiO			0.05	0.18	0.18	0.03	0.18	0.18	0.09	0.09	0.03	0.18	0.18	0.18	0.18	0.18	0.18	0.18	0.18	0.09	0.09	0.18	0.18	0.18	0.18	0.18	0.18	0.18	0.18	0.18	0.09
	TOTAL	96.43	96.16	96.64	96.22	96.83	95.22	98.59	95.56	97.99	98.43	98.86	99.56	98.52	97.86	98.82	98.15	98.26	97.45	97.88	98.86	99.56	98.52	97.86	98.82	98.15	98.26	97.45	97.88	98.86	99.56	

**Table 2** Whole-rock chemical compositions derived from juvenile lapilli from pyroclastic deposits of the Orakei maar

Field no	IKS-801	IKS-802	IKS-804	IKS-805	IKS-806	IKS-807	IKS-808	IKS-809	IKS-810	IKS-811	IKS-812	IKS-813	IKS-814	IKS-815	IKS-817	IKS-818	IKS-819	IKS-820	IKS-821	IKS-822	IKS-823	
wt%																						
SiO <sub>2</sub>	42.94	41.44	42.51	42.16	44.20	43.49	44.39	44.55	40.78	43.14	43.40	42.71	43.96	42.60	43.25	43.37	43.50	42.52	43.83	40.98	45.28	
TiO <sub>2</sub>	3.05	3.13	3.09	3.11	3.02	3.03	3.09	3.09	3.27	3.00	2.97	3.09	2.98	3.10	3.11	3.10	3.05	3.09	2.98	3.36	2.97	
Al <sub>2</sub> O <sub>3</sub>	12.07	11.80	11.75	11.90	11.73	11.69	12.18	12.24	11.65	11.81	11.92	11.81	11.90	11.82	11.82	12.18	12.06	11.76	11.99	11.99	12.08	
Fe <sub>2</sub> O <sub>3</sub>	2.43	2.46	2.43	2.45	2.42	2.39	2.44	2.44	2.56	2.37	2.34	2.45	2.34	2.43	2.45	2.41	2.42	2.43	2.36	2.62	2.32	
FeO	12.13	12.31	12.13	12.24	12.09	11.94	12.20	12.18	12.80	11.84	11.72	12.25	11.71	12.14	12.25	12.03	12.12	12.13	11.81	13.09	11.60	
MnO	0.23	0.21	0.21	0.21	0.20	0.20	0.21	0.21	0.22	0.20	0.20	0.21	0.20	0.21	0.21	0.20	0.21	0.21	0.20	0.20	0.21	
MgO	8.70	8.80	9.11	9.23	8.90	8.72	9.08	9.01	8.84	8.90	8.99	8.88	9.20	9.46	8.26	9.53	8.63	9.45	8.25	8.81	9.40	
CaO	10.26	10.24	10.31	10.35	9.73	10.24	10.21	10.17	10.46	10.10	9.96	10.22	10.18	10.44	10.06	10.60	9.94	10.50	9.81	10.65	9.50	
Na <sub>2</sub> O	3.32	4.43	3.69	3.66	3.12	3.41	2.08	1.93	4.56	4.08	3.55	3.83	3.37	3.40	4.05	2.41	3.56	3.68	4.32	4.14	2.69	
K <sub>2</sub> O	1.69	1.94	1.69	1.89	1.48	1.55	1.12	1.08	1.70	1.83	1.89	1.80	1.38	1.70	1.69	1.41	1.67	1.56	1.87	1.30	1.25	
P <sub>2</sub> O <sub>5</sub>	1.12	1.14	1.14	1.10	1.05	1.08	1.16	1.17	1.24	1.11	1.03	1.14	1.05	1.09	1.18	1.05	1.11	1.13	1.08	1.26	0.95	
LOI + H <sub>2</sub> O	1.64	1.66	1.65	1.66	1.65	1.64	1.67	1.63	1.73	1.60	1.59	1.67	1.59	1.62	1.68	1.63	1.65	1.64	1.60	1.76	1.53	
total	99.57	99.56	99.71	99.96	99.58	99.39	99.83	99.69	99.81	99.99	99.57	100.07	99.86	100.01	100.01	99.92	99.91	100.09	100.11	100.16	99.78	
Mg/No	56.11	56.03	57.23	57.34	56.75	56.54	57.01	56.87	55.18	57.25	57.75	56.36	58.33	58.13	54.57	58.54	55.93	58.12	55.45	54.54	59.09	
ppm																						
Be	2.94	3.27	3.18	3.16	3.12	2.91	3.45	3.14	3.37	2.88	2.95	3.34	2.92	3.08	3.15	2.86	3.05	3.31	3.28	3.51	2.79	
Cs	0.71	0.55	0.45	0.50	0.45	0.59	0.41	0.50	0.44	0.64	0.68	0.58	0.66	0.50	0.69	0.57	0.68	0.54	0.67	0.33	0.45	
Ba	544.70	440.73	517.13	469.65	587.36	627.51	547.26	544.76	413.35	485.18	465.88	500.64	525.64	488.67	558.44	593.77	539.83	475.76	452.98	435.47	456.00	
Rb	31.15	31.06	28.22	30.93	25.47	27.97	20.90	20.30	26.14	30.54	31.64	30.21	21.62	28.51	26.75	24.76	27.91	28.19	33.20	22.49	19.90	
Sr	918.74	981.32	989.96	995.69	911.76	978.08	927.60	896.11	1063.43	973.96	960.42	1048.80	906.57	938.52	1097.00	872.48	970.90	989.48	1017.49	1051.07	672.23	
Pb	10.32	5.31	7.26	6.93	11.69	15.76	8.74	10.61	7.92	8.51	8.53	8.09	5.48	4.97	6.97	6.34	6.41	14.09	10.55	15.46	13.76	
Th	7.99	7.64	8.13	7.64	8.09	8.23	8.52	8.45	8.51	7.99	7.89	8.26	7.45	7.27	8.37	7.30	7.75	7.64	8.08	8.44	7.37	
U	2.31	2.43	2.22	2.31	2.11	2.19	2.11	2.18	2.31	2.39	2.22	2.23	2.16	2.01	2.29	2.03	2.33	2.55	2.60	1.78	1.79	
Zr	342.71	324.15	336.70	320.56	330.84	326.53	346.03	333.78	356.21	319.72	320.29	355.27	305.51	308.11	355.83	307.63	321.69	319.15	359.95	355.81	300.49	
Nb	90.13	92.80	95.48	94.13	91.06	92.33	94.19	92.34	102.91	89.86	89.02	98.22	87.50	88.67	98.86	87.43	92.04	91.75	92.54	104.74	84.27	
Hf	7.05	6.94	7.43	6.98	7.36	6.82	7.58	7.29	7.60	7.26	6.69	7.75	6.49	6.52	7.38	6.57	7.11	6.83	7.87	7.44	6.66	
Ta	5.77	6.02	6.02	6.10	5.89	6.06	6.31	6.12	6.69	6.11	5.89	6.37	5.45	5.75	6.34	5.58	5.84	6.25	6.03	6.69	5.37	
Y	23.71	22.44	24.52	23.06	25.39	24.90	26.10	25.49	24.40	23.48	23.44	23.93	23.52	22.85	24.39	24.55	22.72	24.22	23.38	25.24	23.70	
Sc	17.35	15.35	17.59	16.81	17.53	17.46	18.32	18.26	14.77	16.79	17.21	16.70	17.37	17.31	14.71	18.80	16.01	17.54	15.89	14.67	18.63	
V	245.81	232.03	239.70	242.91	241.83	240.05	246.14	247.27	231.52	231.71	230.38	228.54	241.21	244.46	234.39	256.88	241.05	249.75	224.36	239.56	249.90	
Cr	183.70	153.66	192.63	184.90	175.63	173.90	178.99	177.62	135.55	172.62	185.91	159.66	193.25	192.99	133.12	221.25	160.15	200.75	149.02	133.26	226.40	
Co	70.49	104.26	80.53	98.42	73.61	79.40	71.71	68.31	78.81	65.16	71.63	66.12	66.62	65.33	63.49	62.21	61.10	68.73	72.55	71.05	70.51	
Ni	154.68	139.11	165.98	157.62	164.41	158.26	156.94	156.97	128.93	137.66	141.25	128.91	150.74	147.16	114.80	159.32	124.43	145.86	117.34	122.27	153.11	

Table 2 (continued)

Field no	IKS-801	IKS-802	IKS-804	IKS-805	IKS-806	IKS-807	IKS-808	IKS-809	IKS-810	IKS-811	IKS-812	IKS-813	IKS-814	IKS-815	IKS-817	IKS-818	IKS-819	IKS-820	IKS-821	IKS-822	IKS-823
Cu	62.07	51.87	58.26	55.95	48.50	49.28	50.26	48.73	54.02	59.95	52.05	57.82	41.38	41.32	40.26	49.14	42.31	50.50	50.06	49.13	48.70
Zn	167.58	150.49	153.22	162.58	154.99	164.89	157.69	160.67	168.68	191.44	167.07	177.45	138.85	137.73	163.18	147.67	145.88	127.97	126.92	144.18	118.21
Ga	23.52	23.01	23.84	23.92	23.09	22.78	23.74	23.04	24.01	22.35	22.27	23.82	22.49	23.15	24.07	22.95	23.48	23.29	24.10	25.18	22.88
La	65.82	66.84	70.00	66.07	68.07	68.49	72.00	70.25	75.02	65.89	65.88	72.28	63.49	64.32	73.06	65.23	66.02	67.56	68.06	77.29	62.50
Ce	129.78	131.70	134.54	136.30	130.32	133.11	134.35	133.09	145.84	127.55	128.45	142.09	122.26	131.44	144.02	128.36	133.27	132.67	137.06	151.66	124.21
Pr	14.75	15.01	15.43	15.15	15.14	15.44	15.92	15.43	16.74	14.73	14.39	16.01	14.17	14.61	16.27	14.60	14.76	14.91	15.03	16.69	13.76
Nd	58.27	58.87	62.39	59.49	60.41	60.52	64.78	62.97	65.65	58.29	57.31	63.73	56.73	57.96	63.57	58.68	60.13	60.22	59.49	69.16	56.58
Sm	11.31	11.39	11.63	11.28	11.45	11.93	11.94	12.00	12.61	11.26	10.86	11.84	10.85	10.63	12.36	11.10	10.99	11.87	11.12	12.68	10.60
Eu	3.48	3.54	3.66	3.66	3.61	3.57	3.83	3.62	3.90	3.53	3.36	3.65	3.42	3.33	3.75	3.42	3.40	3.58	3.44	4.01	3.31
Gd	8.88	9.13	9.94	9.00	9.75	9.48	9.55	9.74	9.74	8.74	9.39	9.67	8.40	8.81	9.69	8.86	8.53	9.49	8.91	10.09	9.07
Tb	1.10	1.12	1.13	1.08	1.19	1.21	1.23	1.25	1.17	1.13	1.16	1.28	1.09	1.14	1.30	1.12	1.17	1.19	1.14	1.25	1.12
Dy	5.75	5.66	6.18	5.88	6.18	6.11	6.47	6.44	6.05	5.93	6.02	6.10	5.98	5.75	6.31	5.95	5.72	6.18	6.31	6.50	5.76
Ho	0.91	0.90	0.98	0.90	0.98	0.97	1.05	0.99	0.94	0.98	1.00	1.00	0.85	0.90	0.96	0.99	0.90	0.99	0.93	0.96	0.94
Er	2.20	1.99	2.29	2.16	2.25	2.23	2.36	2.21	2.16	2.16	2.14	2.36	2.11	2.10	2.19	2.25	2.09	2.12	2.10	2.11	2.10
Tm	0.26	0.24	0.29	0.25	0.27	0.27	0.28	0.27	0.25	0.27	0.26	0.28	0.22	0.27	0.26	0.26	0.24	0.29	0.27	0.26	0.29
Yb	1.51	1.42	1.42	1.29	1.44	1.50	1.51	1.52	1.32	1.40	1.38	1.40	1.41	1.28	1.38	1.54	1.36	1.60	1.32	1.40	1.41
Lu	0.19	0.16	0.19	0.19	0.19	0.20	0.20	0.17	0.14	0.19	0.18	0.17	0.19	0.17	0.19	0.19	0.16	0.18	0.17	0.16	0.19

LOI loss on ignition

over 95 wt%, the majority totalling over 98 wt%, which is an acceptable range for basaltic glass compositions. For the whole-rock compositions (Table 2), major and some trace elements were analysed using X-ray fluorescence spectrometry (XRF) and laser-ablation inductively coupled mass spectrometry (LA-ICP-MS). Prior to crushing, rock samples were cleaned and soaked in distilled water then dried at 50 °C and crushed using a tungsten carbide ring grinder. H<sub>2</sub>O was estimated by heating samples to 100 °C and loss on ignition by heating to 1,000 °C. For XRF analysis, 2 g of ignited sample were mixed with 6 g of SPECTRACHEM 12:22 flux and analysed using a Siemens SRS 3000 sequential XRF spectrometer with a Rh tube. For LA-ICP-MS work the fusion discs were mounted in blocks of 30 and polished. Analysis was carried out at the Research School of Earth Science, Australian National University, using a Lambda Physik Complex ArF (193 nm) Excimer LPX120 laser and Agilent 7,500 series mass spectrometer and a VG

Fisons Plasmaquad PQ2. Trace element abundance detection limits are approximately <1 ppb and analytical errors <1 % relative. A BCR standard was analysed for each block of 30 samples. Calibration of samples was provided with the analysis of NIST 612 glass standard and the silica weight percentage determined through XRF analysis was used to correct for variations in ablation.

Orakei pyroclasts are strongly silica undersaturated alkali basalts. Whole-rock compositions of clasts show a tightly restricted range in MgO content (8–10 wt%) and Mg-number (54–59) (100MgO/(MgO + FeO) mol.% Fe<sub>2</sub>O<sub>3</sub>/FeO=0.2), which is at the low end of the range of compositions erupted from the AVF (e.g. McGee et al. 2011). Within this range, SiO<sub>2</sub> content varies between 40 and 45 wt%. Variability of other major elements is limited and correlates with SiO<sub>2</sub> content (Fig. 9).

CaO is generally positively correlated, whereas FeO, Na<sub>2</sub>O and K<sub>2</sub>O are negatively correlated with MgO; Al<sub>2</sub>O<sub>3</sub> and TiO<sub>2</sub> are relatively constant. This compositional range can be described in terms of an evolutionary spectrum between a relatively high Mg and Si end-member, with lower incompatible elements (LILE, HFSE, U, Th, Pb) and higher compatible element contents (Ni, Cr) and a low Mg–Si end-member, with relatively high incompatible element and lower compatible element abundances. These trends are consistent with trends observed at other Auckland volcanoes (Smith et al. 2008; Needham et al. 2011); however, the range of compositions is much smaller at Orakei and samples lie at the most evolved end of the AVF compositional spectrum. The glass compositional range is generally well correlated with whole-clast compositions. The main difference between the behaviour of major elements in ground-mass glass and the whole-clast compositions is the negative correlation of Al and Si with Mg in the glass.

In studies of other centres in the AVF (Smith et al. 2008; Needham et al. 2011) and similar volcanic fields (Brenna et al. 2010), a clear correlation between stratigraphic position and chemical composition has been interpreted in terms of the behaviour of magmas as they crystallise and fractionate at both high and low pressure. In general, erupted products become less evolved upward in a stratigraphic sequence and this has been interpreted as the sequential eruption of a fractionated magma column (Smith et al. 2008). Figure 10 shows, however, that there are no clear compositional trends between characteristic element abundances vs. stratigraphic position in the Orakei tuff. The limited extent of available sections prevents the definitive correlation of stratigraphic position. There is a subtle trend for incompatible element abundances to decrease upward in the succession and this is consistent with the much clearer trend observed in other AVF centres (Smith et al. 2008; Needham et al. 2011). It is also apparent that the elemental abundances show strong scatter about the poorly defined trend.

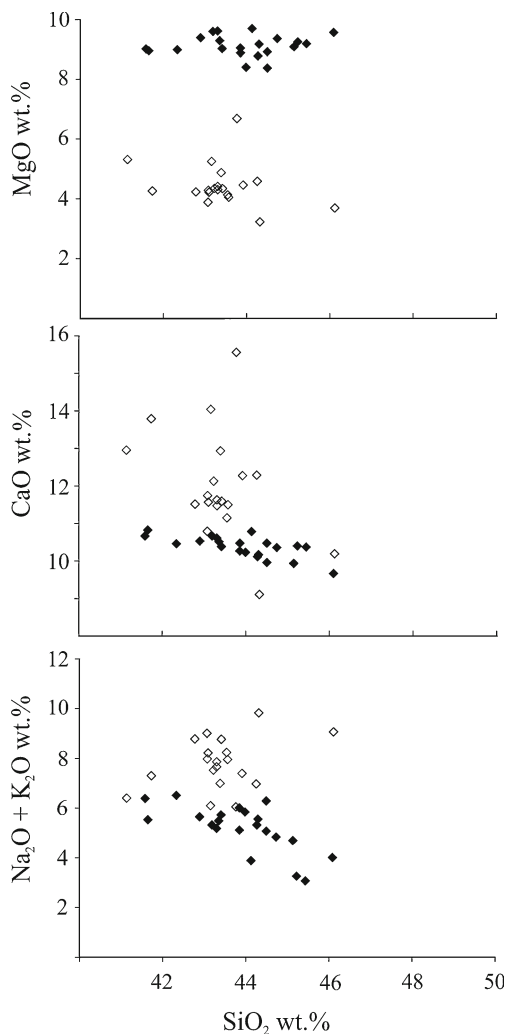
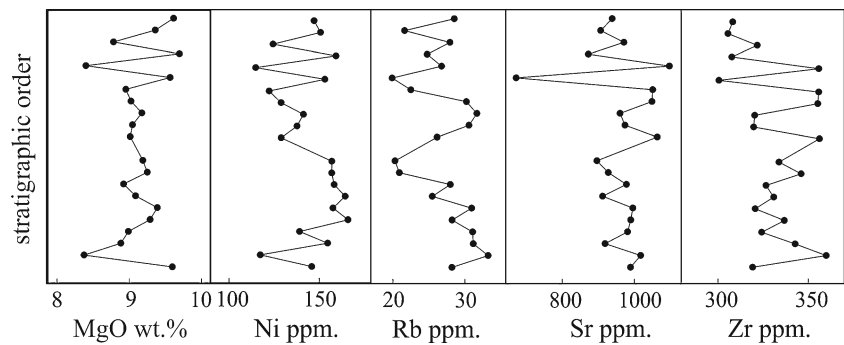


**Fig. 9** Plot of selected major element (oxide) compositions versus SiO<sub>2</sub> (Harker diagrams). *Solid symbols* are juvenile pyroclasts (lapilli size) while *open symbols* are glass compositions (ash size)

**Fig. 10** Plots of selected elements versus their approximate stratigraphic position in the Orakei tuff ring sequence in which no systematic compositional trends can be recognized



### Geochemical interpretation

The discordance between glass and whole-clast chemical compositions is explained by glass compositions being affected by late-stage crystallization of microlites, whereas whole-clast compositions reflect deeper (source or conduit) processes of crystallization and fractionation. To a first order, the relative correlations seen in major elements in whole-clast compositions, with Fe enrichment and constant Al, can be attributed to crystallisation and removal of Fe-poor aluminous clinopyroxene. Experimental work has demonstrated that clinopyroxene crystallises at high pressures from basanitic liquids (Bultitude and Green 1971) and deep-seated fractionation has been proposed for Crater Hill in the AVF (Smith et al. 2008). If the whole-clast variation preserves the signature of deep fractionation that is decoupled from shallow crystallisation processes, magma rise must have occurred rapidly and interaction between compositionally different batches must have been minor.

The variability within the Orakei spectrum of compositions within any one stratigraphic interval is interpreted to result from clast recycling during eruption. This variation is, however, mainly confined to the upper sampled beds. In the lower tuff ring samples, chemical variability is less noticeable and compositional trends are smoother. This may indicate a more stable beginning to the eruption with a greater magmatic flux, giving rise to less mixing and reworking, followed by a waning flux, which allowed greater degrees of mixing and reworking. In addition, a progressive widening of the conduit (as also indicated by unconformities described above) may have caused inward collapse of the crater wall and proximal tephra ring as well as recycling of the earlier accumulated pyroclastic deposits. There is also a large compositional difference in samples separated by a truncation surface at location b (Figs. 2 and 10), which supports the idea of vent widening and particle recycling in later stages of the eruption.

Most significantly, the geochemical dataset indicates a very small range of compositions compared with other AVF centres, while deposit volumes indicate a very small magma volume. The chemistry suggests that Orakei was formed by

eruption of the more-evolved portion of a single small magma batch.

### Discussion of eruption styles

The upper tuff sequence is thickest toward the ENE, which may reflect the paleo-wind direction or the vent geometry. The maximum thickness of the tuff is ~20 m, although it may have been thicker before the crater was expanded by inward wall collapse. An absence of inward dipping proximal deposits can be explained by slumping along concentric faults into the crater. This process would also explain the recycling of previously erupted clasts indicated by the chemical variability. Crater wall collapse and slumping is a common phenomenon in the steep inner crater wall of maars (e.g. Pirrung et al. 2008). The settling of diatreme material beneath a maar basin could also result in enlargement of the maar basin (e.g. Suhr et al.

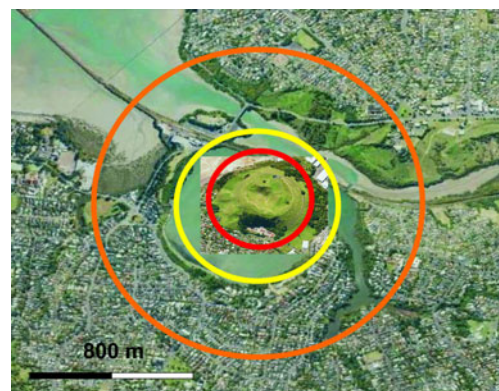


**Fig. 11** Comparison of the “magmatic footprint” in the form of a scoria cone if the same amount of magma that produced Orakei maar would have erupted in the place of Orakei basin without phreatomagmatic explosivity. The estimated geometrical extent of the original size of Orakei maar marked by *yellow* (crater) and *orange* (base of tuff ring), while a *red circle* represents an equivalent scoria cone about 500 m across. An *inset image* of an Auckland scoria cone (e.g. Mount Wellington) shows a graphic comparison to Orakei maar indicating about a magnitude less area could have been affected if no phreatomagmatism would had occurred during the formation of Orakei basin

2006). Crater wall widening could also have been accelerated by wave action in the maar lake over tens of thousands of years (e.g. Gebhardt et al. 2011).

Assuming an original 800-m-wide maar, surrounded by a 20-m-high tephra rim, extending a further 400 m radially (Fig. 11), a maximum total tuff ring volume of 0.013 km<sup>3</sup> is estimated. Little evidence of the tuff ring remains in the northern sector, where pyroclastic deposits were emplaced in and then eroded from a steep valley side, hence the ring's initial volume could have been lower than that of the concentric tuff ring assumed for the volume estimate.

The Orakei tuff is primarily composed of non-volcanic particles ranging from fine-ash grade up to blocks of 0.5 m diameter. The proportion of juvenile clasts varies with grain-size in the lapilli tuff and fine tuff beds that dominate the pyroclastic sequence. Fine-ash fractions contain >90 vol.% particles derived from the sedimentary substrate, whereas lapilli and coarse ash fragments are mostly juvenile. Due to the variable juvenile content of beds in different parts of the tuff ring only an approximate combined volume estimate of the magma erupted can be made. Assuming an overall average of 30 vol.% juvenile particles, the eruption could have involved <0.004 km<sup>3</sup> juvenile ejecta, equating to <0.003 km<sup>3</sup> of DRE magma (assuming a conservative 25 % vesicularity for the pyroclasts based on micro-textural observations) (Fig. 10). No residual gravitational or magnetic anomaly is preserved, pointing to an absence of a lava-fill or juvenile-clast rich diatreme (Cassidy et al. 2007). This volume is around half of that estimated for the Ukinrek Maar eruption in the Alaska Peninsula (0.0057 km<sup>3</sup>; Kienle et al. 1980; Ort et al. 2000). The two maars produced at Ukinrek have diameters of 170 and 300 m, with depths of 35 and 70 m, respectively (Kienle et al. 1980). The Orakei maar crater is at the very least 80 m deep, based on drill cores through maar lake sediments that did not reach the volcanic substrate. Estimation of the potential excavation depth at Orakei based on an inverse conical geometry and the estimated volume of accidental fragments in the tuff ring, results in a crater at least 400 m in radius that could have been up to 155 m deep (Fig. 10).

The geochemical evidence supports a very small magma volume and suggests that only the evolved tip of a small magma batch was involved in this eruption. Particle shapes and textures suggest that concurrent phreatomagmatic and magmatic gas-driven fragmentation occurred throughout the eruption, but with varying degrees of relative dominance. This is similar to the eruption conditions inferred from the Asososca maar, Nicaragua (Pardo et al. 2009). Magma flux and the geometry of its contact with water and mud must have been finely balanced to maximise the efficiency of explosive eruptions, which produced dominantly wet base surges as evidenced from the fine-grained nature of the pyroclastic succession through the entire preserved tuff ring

sequences beside the basal tuff breccia horizons exposed in the NW side of the tuff ring. Periodic higher-intensity pulses of magma supply produced intercalated lapilli tuffs with higher juvenile concentrations in the later phases of the eruption. However, the magma flux never rose to the point where it overwhelmed the influence of the subsurface aquifers. The high-energy and apparently continuous eruption, along with the small total magma volume and its very restricted compositional range, suggests that the Orakei tuff ring was formed very quickly. The two Ukinrek Maars formed over 3 and 7 days (Kienle et al. 1980; Ort et al. 2000). Hence, the Orakei maar eruption could easily have been a week or less in duration.

The phreatomagmatic explosions during the Orakei eruption were confined within the thin shallow weakly indurated Plio/Pleistocene mud, silt (Tauranga Group—a few tens of metres thick—e.g. Edbrooke et al. 2003) and the top of the indurated but fractured Miocene sand- and mudstones (Waitemata Group—a few hundred metres thick, e.g. Edbrooke et al. 2003), which are overlain by finely dispersed Holocene muds and sands from the overlying Pureawa Stream. The Waitemata Group is a flysch-dominated succession of sandstone and mudstone, interbedded with volcanoclastic units (Edbrooke et al. 2003). Many of the layers have low permeability and may act as a barrier to groundwater flow (Russell and Rodgers 1977), although considerable water is stored in fractured zones. Fragments from Waitemata Group units are especially visible in the basal units of the Orakei tuff, showing that initial explosions were located at these depths. The pre-eruptive Pureawa stream valley probably indicates a fractured, weaker zone in the Waitemata group sediments, which likely hosted a pressured aquifer system and perhaps even a deeper structural weakness that was exploited by the rising Orakei magma.

The dune-bedded and finer-grained pyroclastic successions of most of the mid to upper levels of the tuff ring indicate deposition primarily from base surges. The presence of accretionary lapilli-rich beds and vesicular tuffs indicates that these base surges were cool and wet (Lorenz 1974). The ubiquitous presence of mud and fine sand grains throughout these units and trapped blebs of mud within all juvenile clasts of lapilli-size or larger shows that a pulverised country rock mud mixture was probably the main watery phase interacting with the rising magma.

## Conclusions and hazard implications

The Orakei maar is the result of the eruption of a very small volume of relatively evolved mafic magma with an extremely tight compositional range, possibly from the tip of a small dyke system in which magma had fractionated

clinopyroxene at depth. This magma entered into an aquifer in fractured weak mudstone and siltstone sediments located below a stream valley. Explosive magma–water interaction rapidly disrupted the eruptive vent area and fragmented the soft sediments to engender mud–magma interaction that apparently lasted the entire duration of this eruption. Pulsing, highly efficient explosive interactions produced wet base surges depositing tuffs and lapilli tuffs. Mud blebs were intimately mixed within juvenile clasts and disrupted mud/sand particles dominate the  $>2 \phi$  component of the tuffs as well as coating most juvenile particles. Some phases of the eruption showed evidence for higher magma flux with magmatic gas-driven vesiculation and fragmentation producing juvenile lapilli within lapilli tuffs, but phreatomagmatic explosions dominated the eruption dynamics. Crater widening and inward collapse appear to have caused recycling of early juvenile clasts into later base surges, giving rise to mixed juvenile chemical compositions in the uppermost units. The tight compositional range and the lack of major variation in pyroclastic deposition after the opening phase indicates that the eruption was probably brief, lasting less than a week and possibly with the main growth phase taking only a day in a similar fashion to that observed for the Ukinrek maar-forming eruption (e.g. Kienle et al. 1980). The short eruption duration is also supported by the complete lack of erosional surfaces in the most completely preserved tuff ring sequence (mostly in the S, SE side of the maar) that could be indicative of short breaks in the accumulation of tephra around the erupting maar crater.

The Orakei maar is an example of an end-member in the basaltic eruptive spectrum, where the hydrogeological setting determined the eruption style throughout the entire eruption. A maar crater  $>85$  m deep was produced and a total area of  $\sim 3$  km<sup>2</sup> was either excavated/subsided or affected by base surges (Fig. 1). This scenario is one of the most hazardous expected for Auckland City, with a rapid onset of violent explosive activity upon arrival of only a small magma volume. The base surges travelled at least 1.5 km from the vent and tephra fall may have also been important. The Orakei eruption hazards are poorly predictable from its magma volume ( $<0.003$  km<sup>3</sup>), which in the absence of abundant groundwater would have produced a small scoria or spatter cone, having a footprint of  $<0.25$  km<sup>2</sup>. The Orakei eruption footprint is equivalent to the largest scoria cones of the volcanic field such as Mt Wellington or Mt Mangere (Fig. 1b).

The recognition of the hydrogeological control of eruption hazards in a field like the AVF can be used to expand spatio-temporal eruption forecasting models (e.g. Bebbington and Cronin 2011) to include evaluations of potential future eruption style. In the AVF, 36 of the 50 volcanoes had significant explosive phreatomagmatic phases (Allen et al. 1996) (Fig. 1b). Of these, 30 are located

on lowlands such as the Manukau lowland in the south of the field (Fig. 1b) that hosts 16 volcanoes, and the others located along stream valleys (Fig. 1b). The lowland or coastal phreatomagmatic volcanism can be related to thick soft and saturated Quaternary alluvial and estuarine sediments (e.g. the  $\sim 60$  m thick Kawa Formation in the Manukau lowlands; Edbrooke et al. 2003) (Fig. 1b). In cases such as Orakei, fracture-controlled aquifers in Waitemata Group sediments are equally important.

On a more general note, this study has identified the fundamental importance of the “competition” between the magmatic system and the hydrogeology of the eruption site. The essential parameters modulating the eruption outcome are the magma flux, the ongoing availability of water and to a lesser extent the mechanical strength of the country rock. To develop a realistic volcanic hazard scenario matrix for a field like the AVF, a range of factors need to be considered, including: topography, substrate geology, aquifer hydrology, fracture systems and surficial sediment cover.

**Acknowledgements** The authors acknowledge support from the Foundation for Research, Science and Technology International Investment Opportunities Fund, Project MAUX0808 “Facing the challenge of Auckland volcanism” and KN was assisted by the Massey University Research Fund (RM13444). Prof. Claus Siebe and an Anonymous Reviewer provided helpful reviews and we also thank Editors Jeremy Phillips and James White for their contributions toward improving the manuscript.

## References

- Allen SR, Smith IEM (1994) Eruption styles and volcanic hazard in Auckland Volcanic Field, New Zealand. *Geosci Rep Shizuoka Uni* 20:5–14
- Allen SR, Bryner VF, Smith IEM, Ballance PF (1996) Facies analysis of pyroclastic deposits within basaltic tuff-rings of the Auckland volcanic field, New Zealand. *New Zealand J Geol Geophys* 39:309–327
- Auer A, Martin U, Németh K (2007) The Fekete-hegy (Balaton Highland Hungary) “soft-substrate” and “hard-substrate” maar volcanoes in an aligned volcanic complex—implications for vent geometry, subsurface stratigraphy and the palaeoenvironmental setting. *J Volcanol Geotherm Res* 159:225–245
- Bebbington MS, Cronin SJ (2011) Spatio-temporal hazard estimation in the Auckland Volcanic Field, New Zealand, with a new event-order model. *Bull Volcanol* 73:55–72
- Brand BD, Clarke AB (2009) The architecture, eruptive history, and evolution of the Table Rock Complex, Oregon: from a Surtseyan to an energetic maar eruption. *J Volcanol Geotherm Res* 180:203–224
- Brenna M, Cronin SJ, Smith IEM, Sohn YK, Németh K (2010) Mechanisms driving polymagmatic activity at a monogenetic volcano, Udo, Jeju Island, South Korea. *Contr Min Petrol* 160:931–950
- Brown RJ, Branney MJ, Maher C, Dávila-Harris P (2010) Origin of accretionary lapilli within ground-hugging density currents: Evidence from pyroclastic couplets on Tenerife. *Geol Soc Am Bull* 122(1/2):305–320
- Bultitude RJ, Green DH (1971) Experimental study of crystal–liquid relationships at high pressures in olivine nephelinite and basanite compositions. *J Petrol* 12:121–147



- Büttner R, Dellino P, La Volpe L, Lorenz V, Zimanowski B (2002) Thermohydraulic explosions in phreatomagmatic eruptions as evidenced by the comparison between pyroclasts and products from Molten Fuel Coolant Interaction experiments. *J Geophys Res-Solid Earth* 107(B11): art. no.-2277
- Carey S, Maria A, Sigurdsson H (2000) Use of fractal analysis for discrimination of particles from primary and reworked jokulhlaup deposits in SE Iceland. *J Volcanol Geotherm Res* 104:65–80
- Carn SA (2000) The Lamongan volcanic field, East Java, Indonesia: physical volcanology, historic activity and hazards. *J Volcanol Geotherm Res* 95:81–108
- Cassidy J, France SJ, Locke CA (2007) Gravity and magnetic investigation of maar volcanoes, Auckland volcanic field, New Zealand. *J Volcanol Geotherm Res* 159:153–163
- Dellino P, La Volpe L (1996) Image processing analysis in reconstructing fragmentation and transportation mechanisms of pyroclastic deposits. The case of Monte Pilato–Rocche Rosse eruptions, Lipari (Aeolian Islands, Italy). *J Volcanol Geotherm Res* 71:13–29
- Dellino P, Liotino G (2002) The fractal and multifractal dimension of volcanic ash particles contour: a test study on the utility and volcanological relevance. *J Volcanol Geotherm Res* 113:1–18
- Dellino P, Frazzetta G, La Volpe L (1990) Wet surge deposits at La Fossa di Vulcano: depositional and eruptive mechanisms. *J Volcanol Geotherm Res* 43:215–233
- Dellino P, Isaia R, La Volpe L, Orsi G (2004a) Interaction between particles transported by fallout and surge in the deposits of the Agnano-Monte Spina eruption (Campi Flegrei, Southern Italy). *J Volcanol Geotherm Res* 133:193–210
- Dellino P, Isaia R, Veneruso M (2004b) Turbulent boundary layer shear flows as an approximation of base surges at Campi Flegrei (Southern Italy). *J Volcanol Geotherm Res* 133:211–228
- Edbrooke SW, Masengarb C, Stephenson W (2003) Geology and geological hazards of the Auckland urban area, New Zealand. *Quatern Inter* 103:3–21
- Gebhardt AC, De Batist M, Niessen F, Anselmetti FS, Ariztegui D, Haberzettl T, Kopsch C, Ohlendorf C, Zolitschka B (2011) Deciphering lake and maar geometries from seismic refraction and reflection surveys in Laguna Potrok Aike (southern Patagonia, Argentina). *J Volcanol Geotherm Res* 201(1–4):357–363
- Houghton BF, Schmincke HU (1986) Mixed deposits of simultaneous strombolian and phreatomagmatic volcanism; Rothenberg Volcano, East Eifel volcanic field. *J Volcanol Geotherm Res* 30:117–130
- Houghton BF, Wilson CJN, Smith IEM (1999) Shallow-seated controls on styles of explosive basaltic volcanism: a case study from New Zealand. *J Volcanol Geotherm Res* 91:97–120
- Kienle J, Kyle PR, Self S, Motyka RJ, Lorenz V (1980) Ukinrek Maars, Alaska. 1. April 1977 eruption sequence, petrology and tectonic setting. *J Volcanol Geotherm Res* 7:11–37
- Lesti C, Giordano G, Salvini F, Cas RAF (2008) Volcano tectonic setting of the intraplate, pliocene–holocene, newer volcanic province (southeast Australia): Role of crustal fracture zones. *J Geophys Res—Solid Earth* 113(B7): Article #: B07407
- Lorenz V (1974) Vesiculated tuffs and associated features. *Sedimentology* 21:273–291
- Lorenz V (2003) Maar-diatreme volcanoes, their formation, and their setting in hard-rock or soft-rock environments. *Geolines* 15:72–83
- Mandelbrot BB (1967) How long is the coast of Britain? Statistical self-similarity and fractal dimension. *Science* 156:636–638
- McGee LE, Beier C, Smith IEM, Turner SP (2011) Dynamics of melting beneath a small-scale basaltic system: a U–Th–Ra study from Rangitoto volcano, Auckland volcanic field, New Zealand. *Contrib Min Petr* 162(3):547–563
- Molloy C, Shane P, Augustinus P (2009) Eruption recurrence rates in a basaltic volcanic field based on tephra layers in maar sediments: implications for hazards in the Auckland volcanic field. *Geol Soc Am Bull* 121:1666–1677
- Needham AJ, Lindsay JM, Smith IEM, Augustinus P, Shane PA (2011) Sequential eruption of alkaline and sub-alkaline magmas from a small monogenetic volcano in the Auckland Volcanic Field, New Zealand. *J Volcanol Geotherm Res* 201:126–142
- Németh K (2010) Monogenetic volcanic fields: Origin, sedimentary record, and relationship with polygenetic volcanism. In: E. Cañón-Tapia and A. Szakács (Editors), *What Is a Volcano?* GSA Special Papers [Geological Society of America, Boulder, Colorado] 470: 43–67
- Németh K, Cronin SJ (2007) Syn- and post-eruptive erosion, gully formation, and morphological evolution of a tephra ring in tropical climate erupted in 1913 in West Ambrym, Vanuatu. *Geomorphology* 86:115–130
- Ort MH, Wohletz K, Hooten JA, Neal CA, McConnel VS (2000) The Ukinrek maars eruption, Alaska, 1977: a natural laboratory for the study of phreatomagmatic processes at maars. *Terra Nostra* 2000 (6):396–400
- Pardo N, Macías JL, Guido G, Cianfarra P, Avellan DR, Bellatreccia F (2009) The similar to 1245 yr BP Asososca maar eruption: the youngest event along the Nejapa-Miraflores volcanic fault, Western Managua, Nicaragua. *J Volcanol Geotherm Res* 184:292–312
- Pirring M, Buechel G, Volker L, Treutler HC (2008) Post-eruptive development of the Ukinrek East Maar since its eruption in 1977 AD in the periglacial area of south-west Alaska. *Sedimentology* 55(2):305–334
- Ross P-S, White JDL (2006) Debris jets in continental phreatomagmatic volcanoes: A field study of their subterranean deposits in the Coombs Hills vent complex, Antarctica. *J Volcanol Geotherm Res* 149:62–84
- Ross P-S, Delpit S, Haller MJ, Németh K, Corbella H (2011) Influence of the substrate on maar-diatreme volcanoes—an example of a mixed setting from the Pali Aike volcanic field, Argentina. *J Volcanol Geotherm Res* 201:253–271
- Russell WJ, Rodgers KA (1977) Waters of the Western Spring catchment, Auckland. *New Zealand J Marine Freshwater Res* 11:713–728
- Smith IEM, Blake S, Wilson CJN, Houghton BF (2008) Compositional zoning in a small volume monogenetic basaltic volcano in the Auckland volcanic Auckland volcanic field, New Zealand. *Contr Min Petrol* 155:511–527
- Sohn YK, Park KH (2005) Composite tuff ring/cone complexes in Jeju Island, Korea: possible consequences of substrate collapse and vent migration. *J Volcanol Geotherm Res* 141:157–175
- Sohn YK, Cronin SJ, Brenna M, Smith IEM, Németh K, White JDL, Murtagh RM, Jeon YM, Kwon CW (2012) Ilchulbong tuff cone, Jeju Island, Korea, revisited: a compound monogenetic volcano involving multiple magma pulses, shifting vents, and discrete eruptive phases. *Geol Soc Am Bull* 124(3–4):259–274
- Suhr P, Goth K, Lorenz V (2006) Long lasting subsidence and deformation in and above maar-diatreme volcanoes—a never ending story. *Z deutsch Ges Geowissen* 157:491–511
- Valentine GA (1987) Stratified flow in pyroclastic surges. *Bull Volcanol* 49:616–630
- Valentine GA, Gregg TKP (2008) Continental basaltic volcanoes—processes and problems. *J Volcanol Geotherm Res* 177:857–873
- White JDL (1991) The depositional record of small, monogenetic volcanoes within terrestrial basins. In: Fisher RV, Smith GA (eds) *Sedimentation in volcanic settings*. Society for Sedimentary Geology, Tulsa (Oklahoma), pp 155–171
- White JDL, Ross P-S (2011) Maar-diatreme volcanoes: a review. *J Volcanol Geotherm Res* 201:1–29
- Wood CA (1980) Morphometric evolution of cinder cones. *J Volcanol Geotherm Res* 7:387–413